THE USE OF A COHERENT GRADIENT SENSOR IN DYNAMIC MIXED-MODE FRACTURE MECHANICS EXPERIMENTS

J. J. Mason, J. Lambros and A. J. Rosakis

Graduate Aeronautical Laboratories, California Institute of Technology, Pasadena, CA 91125, U.S.A.

Abstract

The use of a coherent gradient sensing (CGS) apparatus is explored in dynamic fracture mechanics investigations. The ability of the method to quantify mixed-mode crack tip deformation fields accurately is tested under dynamic loading conditions. The specimen geometry and loading follow that of Lee and Freund who gave the theoretical and numerical mixed-mode K values as a function of time for the testing conditions. The CGS system's measurements of K_I and K_{II} are compared with the predicted results, and good agreement is found. The method is used to measure K beyond the time domain of the known solution; it is seen that a shift from primarily mode II deformation to primarily mode I deformation occurs.

Nomenclature

K_I, K_{II}	mode I and mode II stress intensity factors
K'	normalization for stress intensity factor
v, E	Poisson's ratio and Young's modulus
σ_{ij}, ε_{ij}, u_i	Cartesian stress, strain and displacement components
$v(t)$	impact velocity
v_o	velocity magnitude
λ	Lame's constant or wavelength of light
c_R, c_S, c_d	Rayleigh, shear and dilatational wave speeds
δS	optical path difference
ε	shearing distance of light beams
Δ	grating separation
p	grating pitch
m, n	integer fringe order
n_o	refractive index of undeformed material
D_1	stress optical constant
h	specimen thickness
l	crack length

1. INTRODUCTION

IN AN EFFORT to understand dynamic mixed-mode crack initiation as well as rapid crack growth, various optical techniques have been used extensively for direct determination of dynamic crack tip fields. The method of photo-elasticity, for instance, has been used to obtain both the dynamic fracture initiation and propagation toughnesses of transient, optically anisotropic materials such as Homalite 100 (DALLY, 1979). The method of caustics, on the other hand, has been used to study dynamic fracture behavior of transient solids such as PMMA and Homalite 100 (THEOCARIS and GDOUTOS, 1972; RAVI-CHANDAR and KNAUSS, 1984) as well as opaque materials such as steel (ROSAKIS and ZEHNDER, 1985). For a review of the method of caustics or the method of photo-elasticity see KALTHOFF (1987b) or BURGER (1987), respectively.

The method of caustics has been used in a variety of fracture mechanics experiments (ROSAKIS and ZEHNDER, 1985; THEOCARIS and GDOUTOS, 1972; RAVI-CHANDAR and KNAUSS, 1984; BEINERT and KALTHOFF, 1981). This technique, however, inherently assumes that the stress field near the crack tip is well described by the dominant $(r^{-1/2})$ singular term of the asymptotic expansion (K-dominance). If the K-dominance approximation is not valid in regions where measurements are performed, the method of caustics can produce erroneous results in its measurement of K_I or K_{II}. Furthermore, if there is limited knowledge of the crack tip deformation field (consider the formation of an adiabatic shear band at a crack tip), the method of caustics can give little information about the deformation. Consequently, a full-field method is experimentally more advantageous because it can offer a more complete description of the deformation and response of the specimen over a larger region and not along a single curve as in caustics. The method of photo-elasticity is a full-field technique, but this method is limited to optically birefringent materials.

The full-field method known as the coherent gradient sensor (CGS) (TIPPUR et al., 1989a, b) is investigated here for the measurement of mixed-mode, dynamic crack tip deformation fields under plane stress conditions in optically transparent, non-birefringent materials. The CGS is a lateral shear interferometer utilizing two identical line gratings. The set up was first proposed for measuring lens abberations (HARI-HARAN et al., 1974; HARIHARAN and HEGEDUS, 1975) but, until recently, other possible applications of the CGS interferometer have been overlooked. When used in fracture mechanics the method gives real time measurements of the inplane stress gradients for transparent materials or the in-plane gradients of the out-of-plane displacements for opaque materials. With data taken at a wide range of points near the crack tip, it is possible for the CGS method both to show whether or not a K-dominant field exist near the crack tip and to find accurate values of K_I and K_{II}.

TIPPUR et al. (1989a, b) have demonstrated the accuracy of the CGS statically for mode I loading; however, its accuracy in dynamic investigations, including dynamic mixed-mode loading, has not been reported.

Recently, KALTHOFF and WINKLER (1987) and KALTHOFF (1987a) have observed interesting behavior in the dynamic propagation of mixed-mode (mostly mode II) cracks in steel. Double-notched specimens were impacted by a projectile travelling with speeds up to 70 m s^{-1} [Fig. 1(a)]. It was found that below a certain impact speed (depending upon the root radius of the notch) dynamic cracks propagated at a

deflected angle of approximately 70° from the notch line. This behavior is to be expected if the material fails in a brittle fashion under a maximum hoop stress criterion (ERDOGAN and SIH, 1963). Above a critical impact speed, however, failure occurs along a direction at a much smaller angle. Further investigation suggests that at high impact speeds (high strain rate) failure occurs in an adiabatic shear banding mode.

An analysis of the experiment of KALTHOFF and WINKLER (1987) and KALTHOFF (1987a) by LEE and FREUND (1990a) shows that both modes of deformation, mode I and mode II, can be expected for such a loading geometry. In fact, apart from the dominant K_{II}, a small negative K_I is also predicted. Lee and Freund indicate limited agreement of the mode II stress intensity factor predicted by their analysis with the caustics measurements of Kalthoff and Kalthoff and Winkler. In these measurements, the caustics patterns were interpreted as corresponding to a pure mode II deformation field. Hence, no values of K_I are reported. The limited agreement of the theoretical results with the experimental measurements may be attributed to a failure of the assumption of K-dominance, which was not thoroughly substantiated in the experiments.

It is important that the Lee–Freund analysis of the experiment be verified so that understanding of the failure mode transition from brittle cracking to adiabatic shear banding can be achieved. Knowledge of the existence and magnitude of a K field at the crack tip could lead to a clearer understanding of the mechanisms behind this failure mode transition.

2. THEORETICAL DEVELOPMENT

2.1. Analytical model

The problem investigated by LEE and FREUND (1990a) is shown in Fig. 1(b). One side of an elastic, half-space containing an edge crack is loaded dynamically by some prescribed velocity, $v(t)$. All other faces are traction-free so the boundary conditions to be satisfied are

$$\left.\begin{aligned}\sigma_{11}(-l, x_2, t) = 0 \\ \sigma_{12}(-l, x_2, t) = 0\end{aligned}\right\} \text{ if } x_2 < 0, \qquad \left.\begin{aligned}\sigma_{12}(-l, x_2, t) = 0, \\ u_1(-l, x_2, t) = \int_0^t v(\tau)\, d\tau\end{aligned}\right\} \text{ if } x_2 > 0,$$

$$\left.\begin{aligned}\sigma_{22}(x_1, 0^\pm, t) = 0 \\ \sigma_{12}(x_1, 0^\pm, t) = 0\end{aligned}\right\} \text{ if } -l < x_1 < 0,$$

and at $t = 0$ all quantities are zero. An elastic plane strain solution to this problem is reported by LEE and FREUND (1990a), but conditions in our experiment are closer to a plane stress situation. As a result, the analysis was adjusted to reflect a plane stress field. This was achieved by substituting for v with the quantity $v/(v+1)$ in the results for K_I and K_{II}. Note that K_I and K_{II} in this problem depend on material constants, namely v, because a velocity boundary condition is prescribed on part of the boundary.
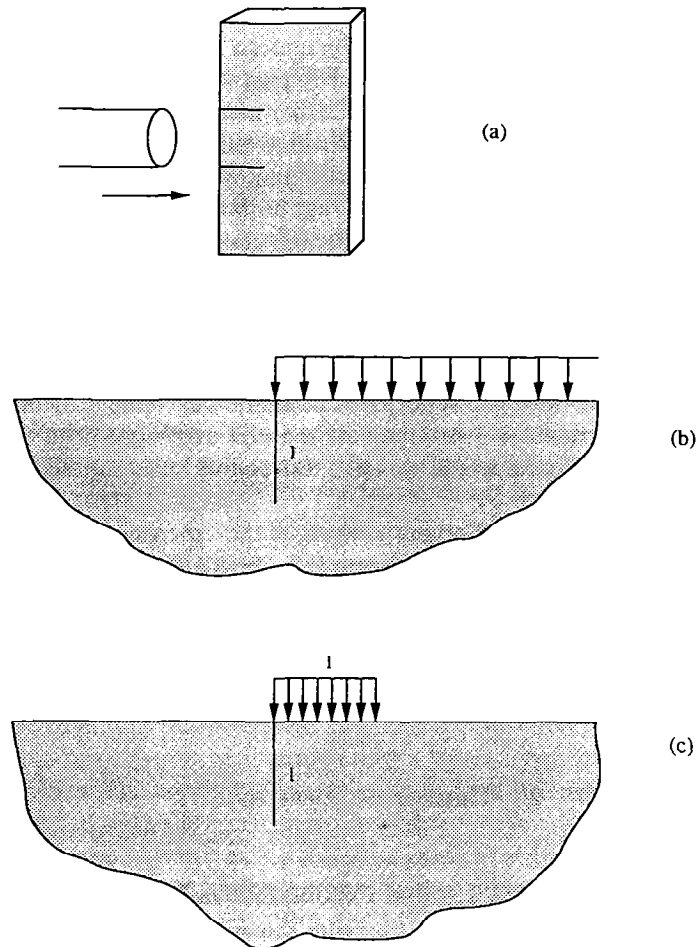
Fig. 1. Loading configuration and geometry for : (a) experiments of KALTHOFF (1989) and KALTHOFF and WINKLER (1987), (b) theoretical solutions of LEE and FREUND (1990a), and (c) finite element solution of LEE and FREUND (1990b).

For PMMA $v \approx 0.35$ and $v/(v+1) = 0.26$; therefore the analysis was evaluated numerically for $v = 0.26$. The normalization factor, K', for the stress intensity factors is given by

$$K' = \begin{cases} \sqrt{\dfrac{l}{\pi}} \dfrac{E v_o}{2 c_d^{p l - \sigma}} & \text{for plane stress,} \\[2em] \sqrt{\dfrac{l}{\pi}} \dfrac{E v_o}{2 c_d^{p l - \sigma}(1 - v^2)} & \text{for plane strain,} \end{cases} \tag{1}$$

where the plane stress normalization factor is found using the above substitution for

(a)

$K_I(t)/K'$

v=0.35 plane stress
v=0.35 plane strain

$c_d t/l$

(b)

$K_{II}(t)/K'$

v=0.35 plane stress
v=0.35 plane strain

$c_d t/l$

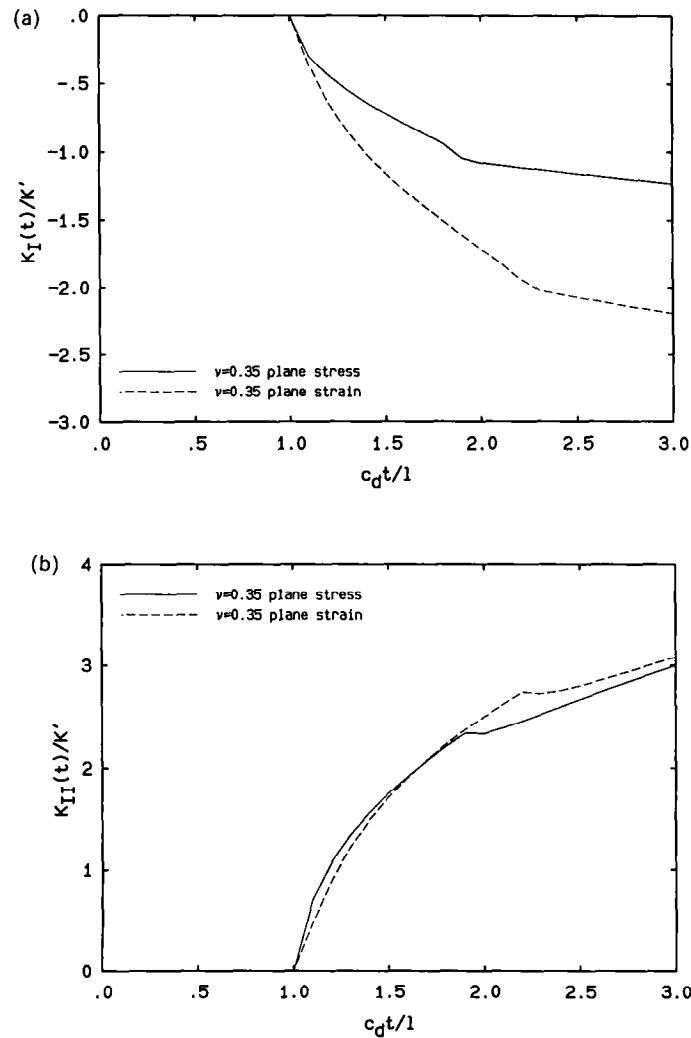Fig. 2. (a) Theoretical predictions for $K_I(t)$ from the analysis of LEE and FREUND (1990a) for $v = 0.26$. (b) Theoretical predictions for $K_{II}(t)$ from the analysis of LEE and FREUND (1990a) for $v = 0.26$.

v in the plane strain normalization factor given by LEE and FREUND (1990a). The time axis is normalized by the characteristic time. $l/c_d^{pl-\sigma}$, where $c_d^{pl-\sigma}$ is the plane stress dilatational wave speed. The results of the new calculations for both mode I and mode II stress intensity factors are shown in Fig. 2(a) and (b), respectively. As expected, these results are very close to the results of LEE and FREUND (1990a) for $v = 0.25$.

Most of the qualitative features of the curves in these figures can be explained. Upon impact a plane compressive wave is generted. It is followed by cylindrical unloading waves generated at the corners of the impact area. The compressive wave gives rise to K_{II}. The existence of the unloading wave makes the increase in K_{II} progressively more gradual and forces the crack faces to close, thus causing a smaller,
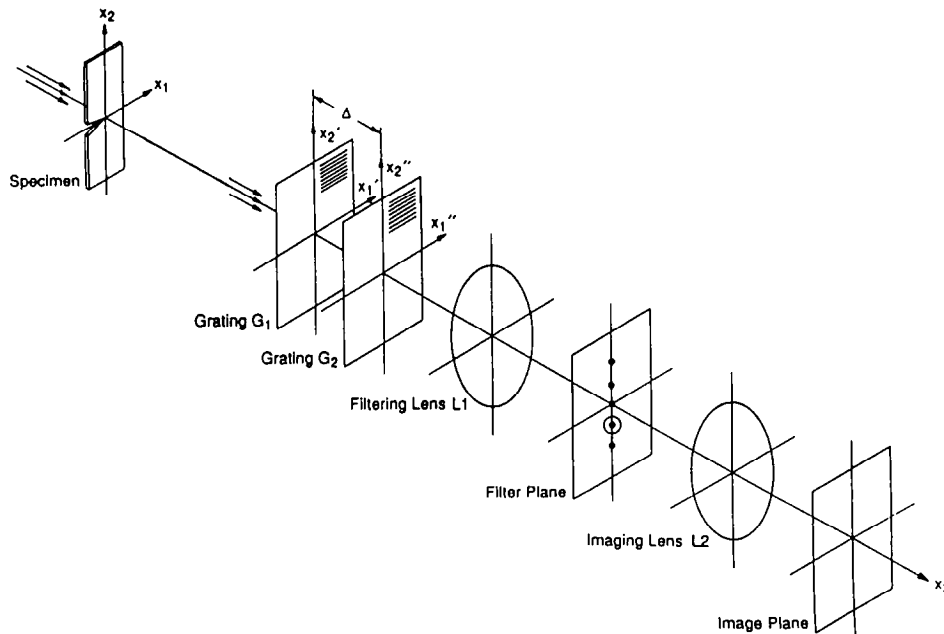
FIG. 3. Schematic of the experimental set up for transmission CGS.

but significant, negative K_1. As can be seen in Fig. 2(a) and (b) there exist three regions in the solution. These correspond to the arrivals at the crack tip of the first dilatational, shear and Rayleigh waves, respectively. The solution is valid up to $c_d t/l = 3$, which corresponds to the arrival of a second dilatational wave that is reflected from the impact surface.

2.2. The method of CGS

In contrast to TIPPUR et al. (1989a, b), the theoretical development of CGS shown here follows the more traditional approach of MURTY (1978) for lateral shearing interferometers. The two approaches are equivalent; the same assumptions are made and the same governing equations result. It is hoped that the more traditional development will result in an easier understanding of the method. A schematic of the set up is shown in Fig. 3. A coherent, collimated laser beam, 50 mm in diameter, passes through a notched transparent specimen. After exiting from the deformed specimen, the beam falls upon the first of two identical diffraction gratings (40 lines/mm). The primary grating splits the beam into a direct beam and numerous diffraction orders. For the sake of brevity, only the first diffraction orders (± 1) and the direct beam are considered. The second diffraction grating diffracts both the direct beam and the first diffraction orders into three beams each, giving a total of nine beams behind the second grating. Of these nine beams the $(0, \pm 1)$ and $(\pm 1, 0)$ orders are parallel—as can be seen in Fig. 4.
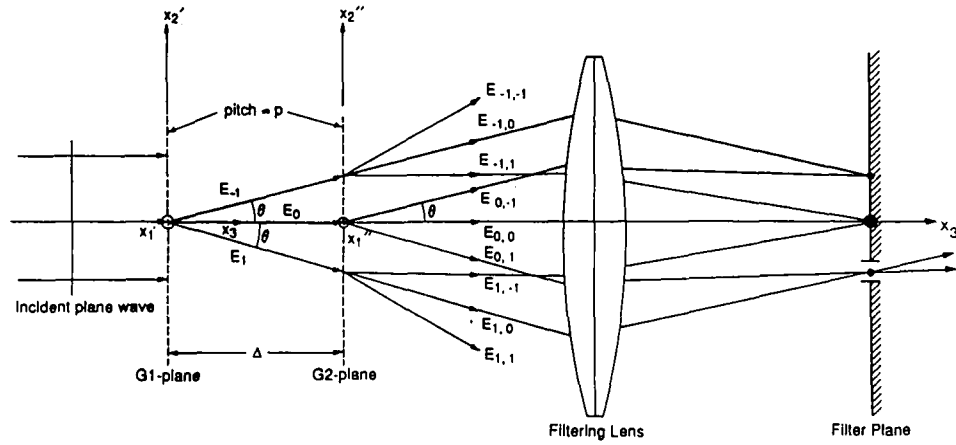
Fig. 4. Schematic describing the working principle of CGS.

An on-line spatial filter is used to isolate one of the two pairs of parallel beams. A lens is placed a distance equal to its focal length behind the secondary grating as in Fig. 3. The Fourier transform of the intensity distribution at the second grating is observed in the back-focal plane of the lens where an aperture is placed on either the +1 or −1 diffraction order spot. The aperture filters all but the two desired parallel beams from the wavefront. Another lens is placed at a distance equal to its focal length behind the aperture to invert the Fourier transformation.

It is assumed that the wave front before the first grating is approximately planar with some phase difference, $\delta S(x_1, x_2)$. Deviations of the propagation direction from the optical axis are neglected. Thus, the two gratings shift one beam with respect to the other by a distance

$$\varepsilon = \Delta \tan \theta \approx \Delta \theta, \tag{2}$$

where Δ is the separation between the gratings (Fig. 3) and θ is the angle of diffraction (assumed small), given here by

$$\theta = \sin^{-1} \frac{\lambda}{p} \approx \frac{\lambda}{p}, \tag{3}$$

where λ is the wavelength of the illumination and p is the pitch of gratings.

The two parallel, sheared wavefronts constructively interfere at a point if their difference in phase is an integer multiple of the wavelength, i.e. if

$$\delta S(x_1 + \varepsilon, x_2) - \delta S(x_1, x_2) = m\lambda, \tag{4a}$$

where m is called "the fringe order". Dividing this equation by ε gives

$$\frac{\delta S(x_1 + \varepsilon, x_2) - \delta S(x_1, x_2)}{\varepsilon} = \frac{m\lambda}{\varepsilon}, \tag{4b}$$

which, for sufficiently small ε, may be approximated by

$$\frac{\partial[\delta S(x_1, x_2)]}{\partial x_\alpha} = \frac{mp}{\Delta}.$$ (5)

In (5), the approximations in (2) and (3) have been used, and the result has been generalized to include shearing in either the x_1- or x_2-direction ($\alpha = 1, 2$).

Equations (4a) and (4b) are the standard equations for lateral shearing inter-ferometry found in MURTY (1978). Note that as ε goes to zero the approximation in (5) grows more exact, but at the same time the number of fringes and, therefore, the sensitivity of the system, is decreased. It is important that the grating separation, Δ, and, consequently, the value of ε, appropriately balances the competition between maximizing sensitivity and approximating the derivative.

For a transparent material, the phase difference, $\delta S(x_1, x_2)$, in (4a) and (4b), is given by the difference in optical path length. Two important factors are included in calculating this parameter; the change in refractive index of the material due to variations in hydrostatic stress, and changes in specimen thickness due to Poisson's contraction. The optical path difference is, thus, given by

$$\delta S(x_1, x_2) = 2h(n_o - 1) \int_0^{1/2} \varepsilon_{33} \, \mathrm{d}\left(\frac{x_3}{h}\right) + 2h \int_0^{1/2} \delta n_o \, \mathrm{d}\left(\frac{x_3}{h}\right),$$ (6)

where n_o is the index of refraction of the un-deformed material and h is the thickness. The first term in (6) represents the optical path difference due to changes in the plate thickness caused by the strain component, ε_{33}. The second term represents the optical path difference accumulated due to stress-induced change in refractive index given by the Maxwell relation

$$\delta n_o(x_1 x_2) = D_1(\sigma_{11} + \sigma_{22} + \sigma_{33}),$$ (7)

where D_1 is the stress-optic constant and σ_{ij} are the Cartesian stress components. Assuming the material is isotropic and linearly elastic, and using the plane stress assumption substitution of (7) into (6), yields (TIPPUR et al., 1989a, b)

$$\delta S(x_1, x_2) \approx \bar{c}h(\hat{\sigma}_{11} + \hat{\sigma}_{22}),$$ (8)

where $\bar{c} = D_1 - (\nu/E)(n_o - 1)$ and $\hat{\sigma}_{11}$ and $\hat{\sigma}_{22}$ are plane stress thickness averages of stress components in the material, while $\hat{\sigma}_{33} = 0$. Finally, substituting (8) into (5) gives the result

$$\bar{c}h \frac{\partial(\hat{\sigma}_{11} + \hat{\sigma}_{22})}{\partial x_\alpha} \approx \frac{mp}{\Delta}.$$ (9)

All interference images produced by the CGS apparatus are interpreted using (9). A similar analysis may be carried out for opaque materials in reflection giving results with the same form (TIPPUR et al., 1989a, b).

For the case of a mixed-mode, K-dominant deformation field at a crack tip,

$$(\hat{\sigma}_{11} + \hat{\sigma}_{22}) = \frac{2}{\sqrt{2\pi r}}\left(K_1 \cos\frac{\phi}{2} - K_{11} \sin\frac{\phi}{2}\right),$$ (10)

where $r = \sqrt{x_1^2 + x_2^2}$ and $\phi = \tan^{-1}(x_2/x_1)$. x_1 and x_2 are the coordinates along the
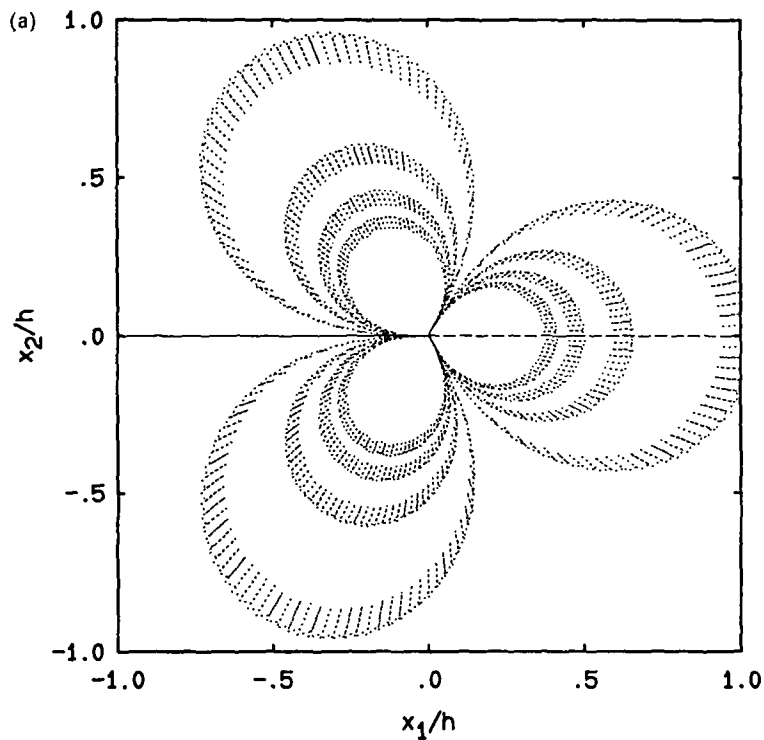
crack length and perpendicular to the crack length, respectively, with the origin at the crack tip. Equation (9) indicates that constructive fringes are formed if

$$A\frac{\sin 3/2(\phi-\psi)}{\sqrt{2\pi r^3}} = \frac{mp}{\Delta \bar{c}h} \quad \text{for } x_1\text{-gradients} \tag{11a}$$
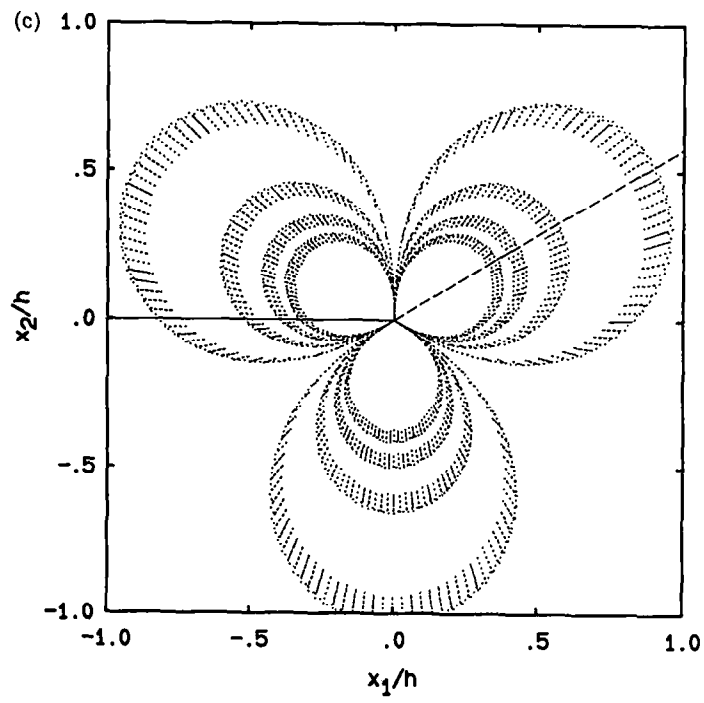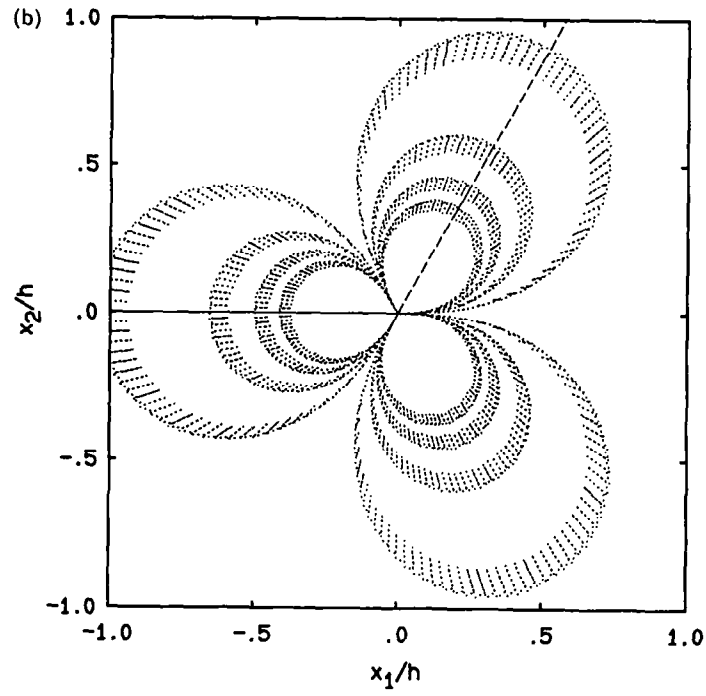
or

$$A\frac{\cos 3/2(\phi-\psi)}{\sqrt{2\pi r^3}} = \frac{mp}{\Delta \bar{c}h} \quad \text{for } x_2\text{-gradients,} \tag{11b}$$

where $K_I/K_{II} = \tan(3\psi/2)$, and $A = K_{II}/\cos(3\psi/2)$. An example of the fringe pattern expected from (11a) is shown in Fig. 5(a) for $K_{II} = 0$ and Fig. 5(b) for $K_I = 0$. A change in the ratio K_I/K_{II} results in a rotation and/or magnification of the fringe pattern, as seen in Fig. 5(c).

Fig. 5. (a) Numerical predictions of CGS fringes {constant $[\partial(\bar{\sigma}_{11}+\bar{\sigma}_{22})]/\partial x_1$ values} constructed on the basis of a pure K_I field. (b) Numerical predictions of CGS fringes {constant $[\partial(\bar{\sigma}_{11}+\bar{\sigma}_{22})]/\partial x_2$ values} constructed on the basis of a pure K_{II} field. (c) Numerical predictions of CGS fringes {constant $[\partial(\bar{\sigma}_{11}+\bar{\sigma}_{22})]/\partial x_2$ values} constructed on the basis of a mixed-mode K field. $K_I = K_{II}$.

(b)

(c)

FIG. 5. *Continued.*
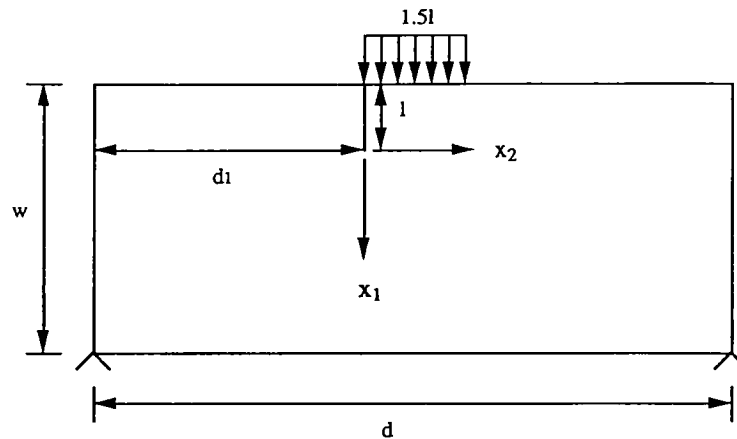
3. EXPERIMENTAL PROCEDURE

3.1. *Apparatus*

The specimen geometry is shown in Fig. 6. Specimens are made of PMMA because it approximates the linear elastic assumption of the theoretical solution. Square tip notches ≈ 1.5 mm thick are cut on a band saw as per Fig. 6. The inclusion of a notch of finite opening rather than a crack allows the generation of a negative mode I stress field at the notch tip (as long as the notch faces do not come into contact). Thus, the mode I response of the system can be investigated.

Impact of the specimens is achieved using a Dynatup drop weight tower. The contact area of the drop weight tup is made of steel, and the corners are rounded to reduce stress concentration. The weight is dropped from approximately 1.4 m, giving it a velocity of 5.25 m s^{-1} at impact. Including the impedance mismatch of the two materials, this results in a contact interface velocity between the specimen and the drop weight of ≈ 5 m s^{-1}.

The set up of the CGS apparatus follows Fig. 3. A streak camera is used as the imaging system. The CGS interferograms are generated using an argon-ion laser pulsed for 50 ns at 7-μs intervals as the light source. The total length of the test is ≈ 300 μs, resulting in approximately 40 CGS interferograms per test.

The fringe patterns are digitized by hand. A ray of constant ϕ from the crack tip is followed; points at the center of fringes are digitized along the way. Most of the

Dimensions of specimen :
l=25mm
w=127mm
d=254mm
d$_1$=136mm
thickness=7.5mm

Mechanical properties of specimen:
E=1240 MPa
v=0.35
c=1.08 10^{-10} Pa
c$_d^{pl-\sigma}$=1765 m/s

FIG. 6. Specimen geometry, loading configuration and material constants.

uncertainty in digitization arises from locating the crack tip and choosing the center of the fringe. Uncertainties in the measurement of ϕ are minimal.

3.2. *Data reduction*

Rearranging (11a) gives

$$\frac{m_i p}{\Delta \bar{c} h} \sqrt{2\pi r_i^3} = Y_i, \tag{12}$$

where $Y_i = A \sin 3/2(\phi_i - \psi)$ and the subscript i refers to individually digitized points. The left-hand side of (12) is obviously constant for fixed ϕ, K_I and K_{II}. If K-dominance is exhibited, plotting the left-hand side of (12) with respect to r should result in a horizontal line. K-dominance was studied by producing such plots and investigating their slope.

Deviation of experimental results from the fringe patterns predicted by a K-dominant field are expected for various reasons. These include the notch tip geometry, the zone around the notch tip where plane stress assumptions break bown (the 3-D zone) (ROSAKIS and RAVI-CHANDAR, 1986; KRISHNASWAMY *et al.*, 1988) and the finite specimen size. Once a region of K-dominance is located, however, a fit of the expected fringe pattern to the digitized data points can be attempted. This fit is produced by minimizing the error function

$$\chi(K_I, K_{II}) = \sum_{i=1}^{N} [r_i^{3/2} - \hat{r}^{3/2}(\phi_i, m_i, K_I, K_{II})]^2, \tag{13}$$

where

$$\hat{r}^{3/2}(\phi_i, m_i, K_I, K_{II}) = \frac{\Delta \bar{c} h}{m_i p \sqrt{2\pi}} \left[K_{II} \sin\left(\frac{3\phi_i}{2}\right) - K_I \cos\left(\frac{3\phi_i}{2}\right) \right] \tag{13a}$$

and N is the total number of points. The minimization of (13) results in a linear set of equations for K_I and K_{II}. It is noted that the function χ inherently weights the outer lobes of the interferograms more strongly than the inner lobes. Another function was tested, namely,

$$\tilde{\chi}(K_I, K_{II}) = \sum_{i=1}^{N} [m_i - \hat{m}(\phi_i, r_i, K_I, K_{II})]^2,$$

where

$$\hat{m}(\phi_i r_i, K_I, K_{II}) = \frac{\Delta \bar{c} h}{p \sqrt{2\pi r_i^3}} \left[K_{II} \sin\left(\frac{3\phi_i}{2}\right) - K_I \cos\left(\frac{3\phi_i}{2}\right) \right].$$

This function weights the inner lobes more heavily, but results similar to those reported here are found.
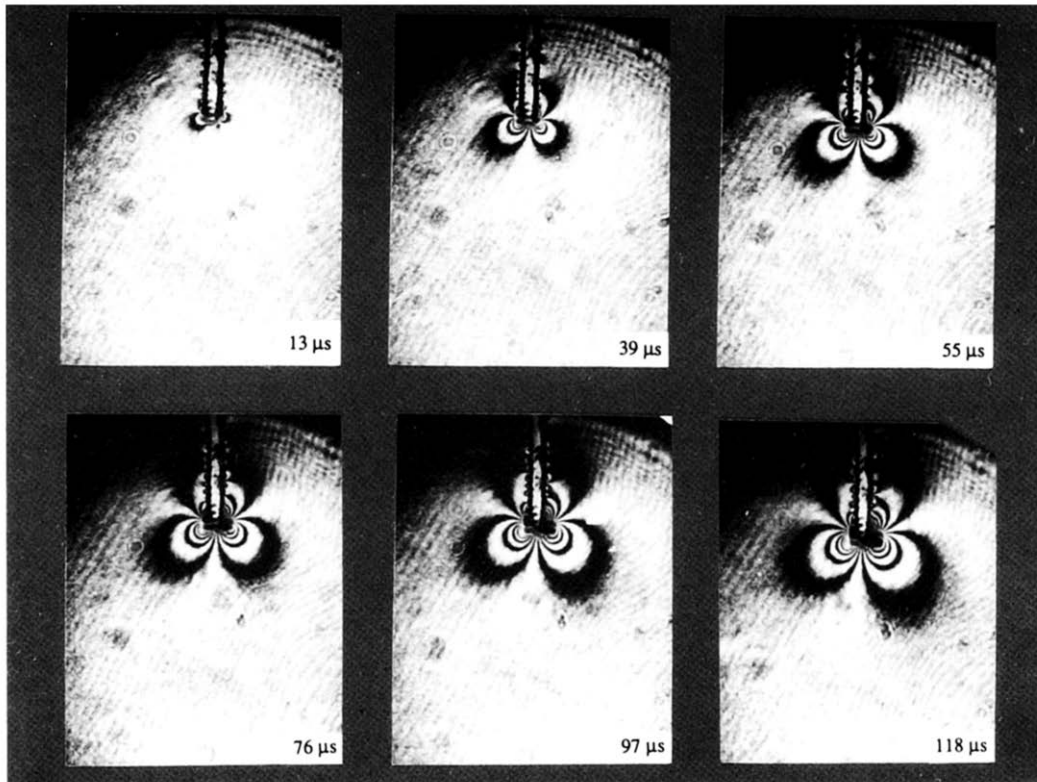
FIG. 7. Sequence of CGS interferograms corresponding to the initial stages of the dynamic asymmetric loading of the pre-notched specimen.
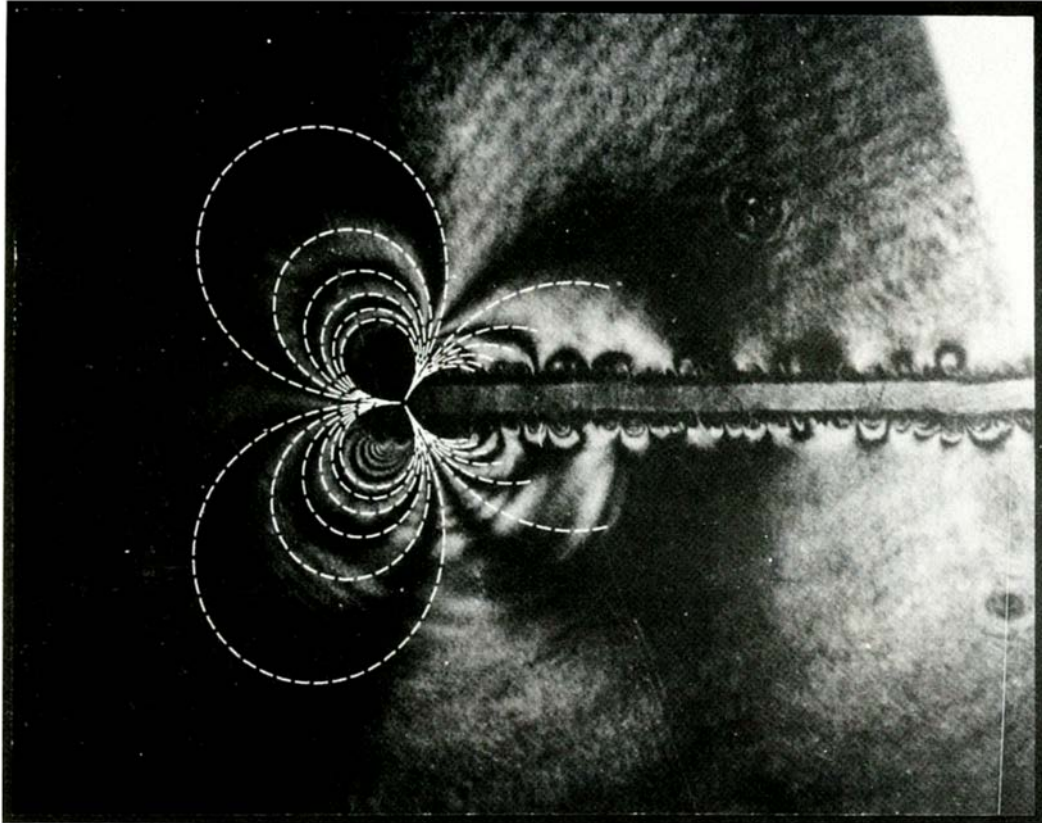
FIG. 9. Synthetic fringe pattern reconstructed from one-term analysis compared with experimental transmission mixed-mode CGS interferogram.
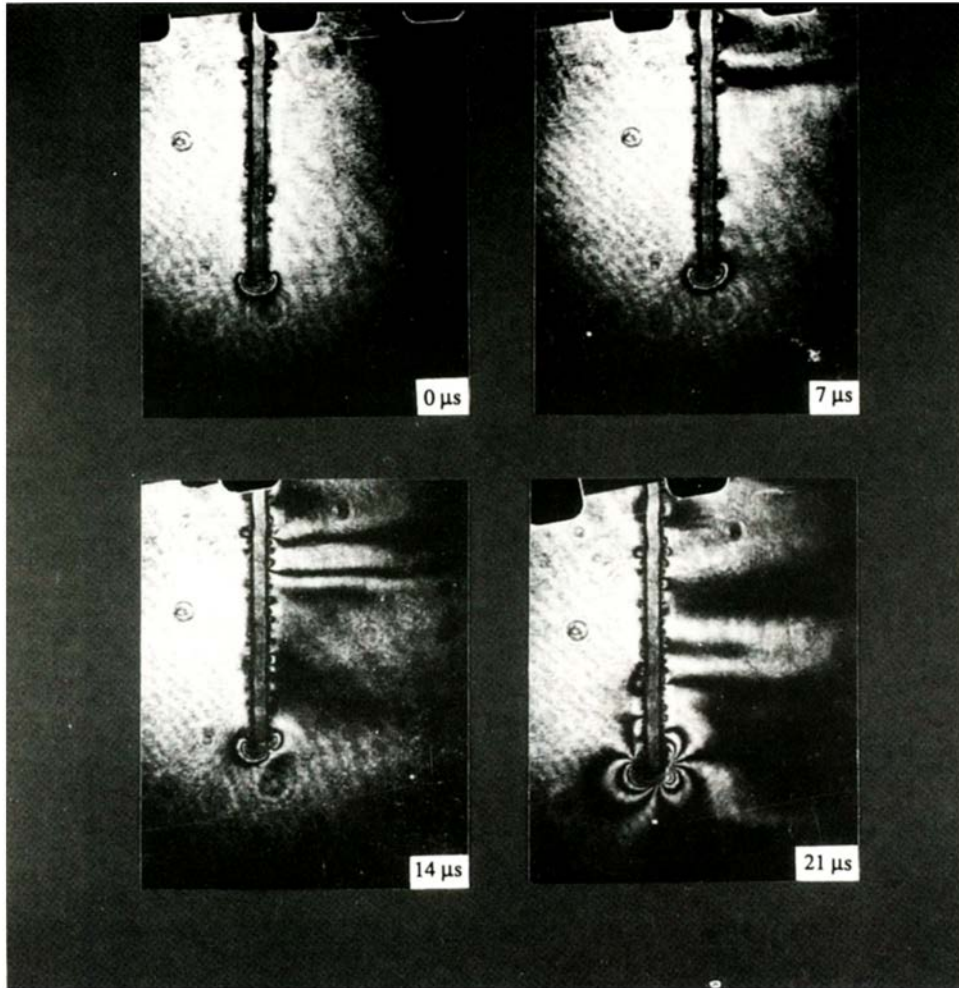
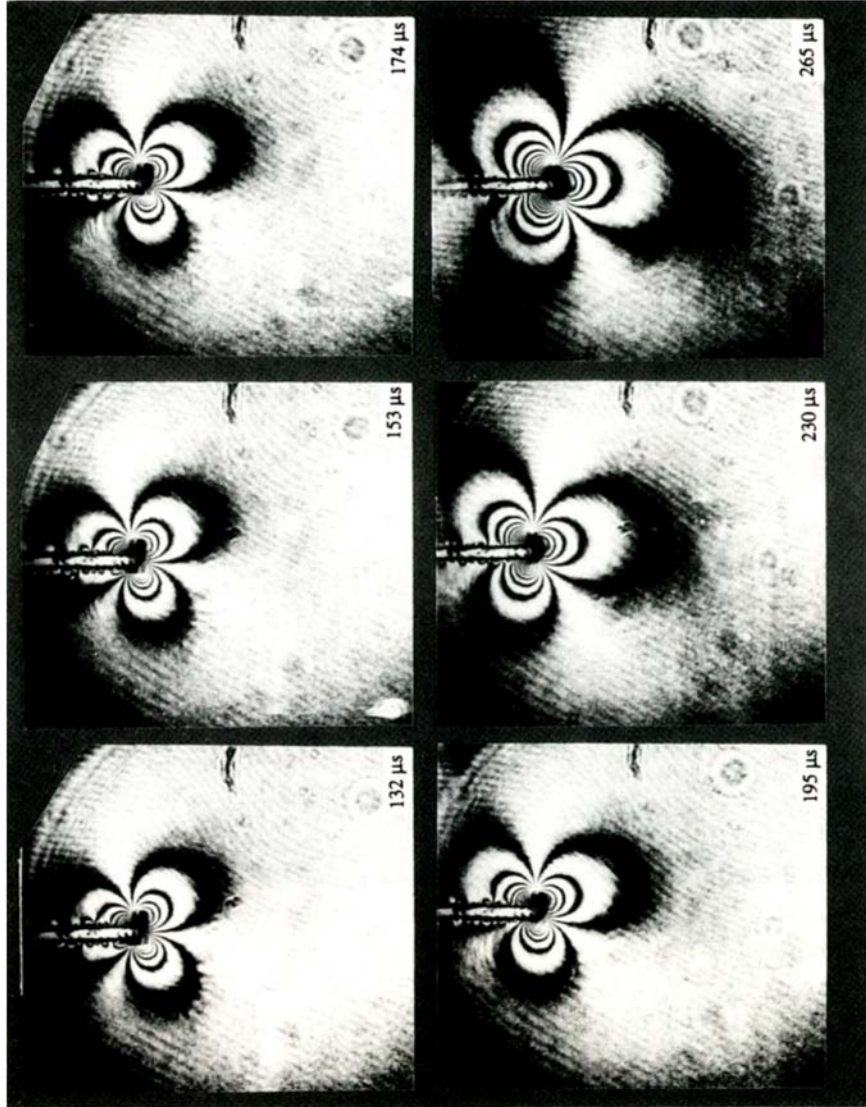FIG. 11. Sequence of high-speed images showing compressive waves generated during impact.

FIG. 12. Sequence of CGS interferograms corresponding to the later stages of the dynamic assymetric loading of the pre-notched specimen.

4. RESULTS AND DISCUSSION

A series of shearing interferograms is shown in Fig. 7. Comparison with Fig. 5(b) shows that the fringes represent a primarily mode II type of deformation at a short time after impact $(c_d t / l \leq 3)$. In analogy to observed near-tip 3-D effects in mode I deformation (ROSAKIS and RAVI-CHANDAR, 1986; KRISHNASWAMY et al., 1988) it is expected that, within a radius equal to half the specimen thickness, mixed-mode deformation will have a strongly 3-D character. As a result, the fringes contained within a radius equal to half the specimen thickness were always excluded in the analysis. Digitization was always performed outside the 3-D zone for the useable interferograms, and, consequently, the results up to 18 μs $(c_d t / l = 1.2)$ were rendered un-interpretable.

Before attempting a fit based on (13), K-dominance was investigated. The left-hand side of (12) was plotted for various values of r_i and constant ϕ. Examples of such plots are shown in Fig. 8. It can be seen in Fig. 8 that in a substantial region surrounding the 3-D zone horizontal lines result. Thus, K-dominance is a reasonable assumption for data points taken beyond half the thickness from the notch-tip.

Fitting of the theoretical fringes to the digitized points was carried out for a K-dominant field, and an example of such fits is shown in Fig. 9. In Fig. 9 the theoretical fringe pattern from the fit has been superimposed on the interferogram from the experiment. It can be seen that the experimental interferogram matches the theoretical fringe pattern quite well. The resulting K values from all the fits are shown in Fig. 10 plotted with the analysis of LEE and FREUND (1990a) and the numerical calculations of LEE and FREUND (1990b). Normalization of the experimental data was achieved using the plane stress values for K' [see (1)]. As can be seen, good agreement between the experiment and the analysis is found. In Fig. 10(a) the mode I experimental results follow the numerical simulation closely, but most deviate from the theoretical analysis. This is expected since the theoretical loading has an infinite area of contact while the
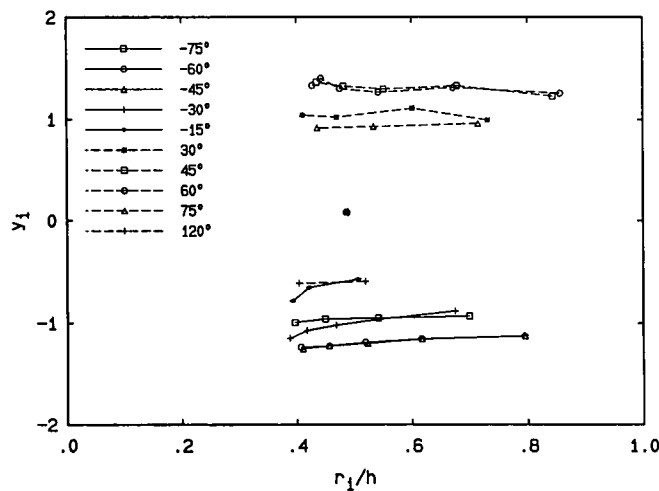

FIG. 8. Radial variation of Y_i for various ϕ at a time, $t = 49$ μs $(c_d t / l = 3.3)$, after impact.
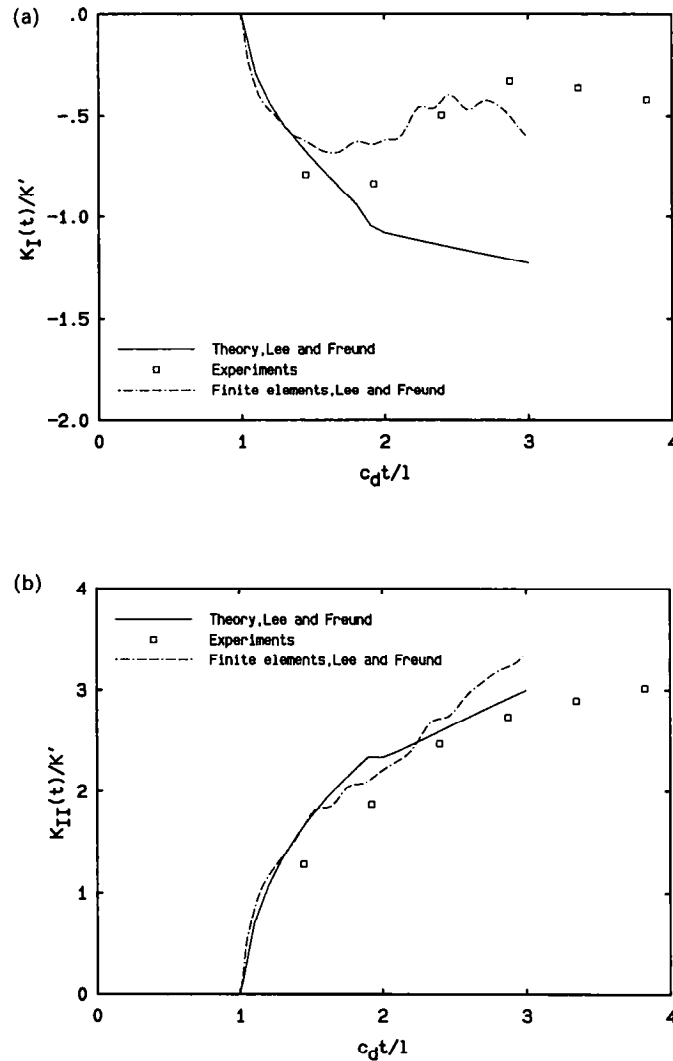
Fig. 10. (a) Normalized stress intensity factor as a function of normalized time for "short" times $(c_d t/l < 3)$. Comparison of theoretical analysis of Lee and Freund (1990a), numerical analysis of Lee and Freund (1990b) and experimental results for mode I. (b) Normalized stress intensity factor as a function of normalized time for "short" times $(c_d t/l < 3)$. Comparison of theoretical analysis of Lee and Freund (1990a), numerical analysis of Lee and Freund (1990b) and experimental results for mode II.

finite element analysis models our specimen more closely. (In this experiment, the area of contact is small, 1.5 times the crack length; the finite element analysis is carried out for loading area equal to the crack length. This effect also explains the large difference between numerical and analytical predictions.) The good agreement of mode I results indicates that the method is sensitive enough to measure both K_I and K_{II} even when the ratio K_I/K_{II} is small. In Fig. 10(b), the mode II results agree well with both the theoretical and the numerical analysis.
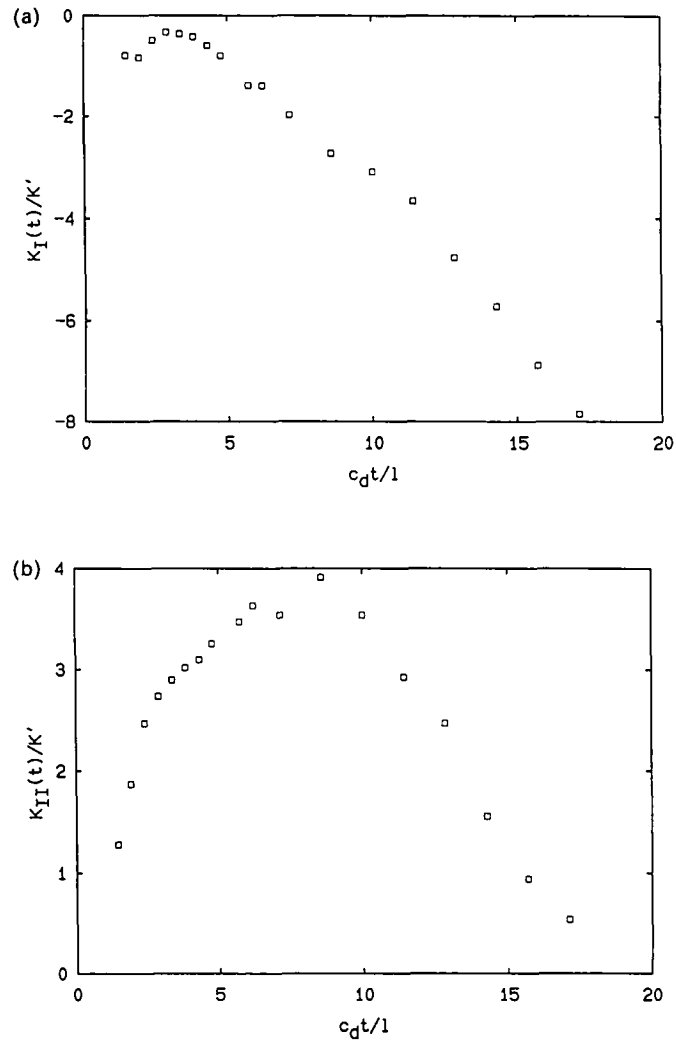
FIG. 13. (a) Normalized stress intensity factors as a function of "long" times $(c_d t/l > 3)$ for mode I. (b) Normalized stress intensity factors as a function of "long" times $(c_d t/l > 3)$ for mode II.

It is noted that experimentally determining the time of impact, i.e. $c_d t/l = 0$, is difficult. Simply watching the tup impact the specimen is not sufficient because in the time between two exposures the tup moves a distance ≈ 1 μm. The magnification is ≈ 1; thus, detecting such small motions is impossible. However, at 5 m s^{-1} impact velocity, it is possible for the CGS to detect the initial compression wave traveling from the contact area to the crack tip (see the interferograms in Fig. 11) and, thus, determine the time of impact. Measurement of the velocity of this wave $(c_d = 1750$ m s$^{-1})$ agrees well with the expected plane stress velocity in PMMA for a dilatational wave. By extrapolating the wave propagation back to the contact area, the time of impact was found satisfactorily.

In the CGS interferograms at later times (Fig. 12) it can be qualitatively seen that a shift from primarily mode II in Fig. 7 to primarily mode I deformation occurs. The fit of K-dominant fringes in this time domain gives the results shown in Fig. 13. The time of the initiation of a mode change, the time when K_{II} reaches a maximum, coincides with the arrival time of the reflected dilatational wave from the opposite side of the specimen, $c_d t/l \approx 9$.

In conclusion, the ability of CGS to measure mixed-mode stress intensity factors under dynamic conditions has been examined. The good agreement between experimental results and theory demonstrates that even when mode-mixity is not substantial, the method produces acceptable values for both stress intensity factors. A shift of dominant deformation mode II to mode I is observed over 300 μs for this loading and specimen geometry. This fact is important in experiments using this configuration. Depending upon the time of initiation and, as a result, the mode-mixity, crack propagation can occur in many different directions.

ACKNOWLEDGEMENTS

REFERENCES

BEINERT, J. and KALTHOFF, J. F.   1981   In *Mechanics of Fracture* (edited by G. SIH), Vol. 7, p. 281. Sijthoff & Noordhoff, Leiden.

BURGER, C. P.   1987   In *Handbook on Experimental Mechanics* (edited by A. S. KOBAYASHI), Chap. 5. Prentice-Hall, Englewood Cliffs, NJ.

DALLY, J. W.   1979   *Exp. Mech.* **19**, 349.

ERDOGAN, F. and SIH, G. C.   1963   *J. basic Engng* **85**, RCR 484-6.

HARIHARAN, P. and HEGEDUS, Z. S.   1975   *Optics Commun.* **14**, 148.

HARIHARAN, P., STEEL, W. H. and WYANT, J. C.   1974   *Optics Commun.* **11**, 317.

KALTHOFF, J. F.   1987a   *Photomechanics and Speckle Metrology*, SPIE Vol. 814, p. 531.

KALTHOFF, J. F.   1987b   In *Handbook on Experimental Mechanics* (edited by A. S. KOBAYASHI), Chap. 9. Prentice-Hall, Englewood Cliffs, NJ.

KALTHOFF, J. F. and WINKLER, S.   1987   In *Impact Loading and Dynamic Behaviour of Materials* (edited by C. Y. CHIEM, H.-D. KUNZE and L. W. MEYER), Vol. 1, p. 185.

KRISHNASWAMY, S., ROSAKIS, A. J. and RAVICHANDRAN, G.   1988   Caltech Report SM88-21 (submitted to *J. appl. Mech.*).

LEE, Y. J. and FREUND, L. B.   1990a   *J. appl. Mech.* **57**, 104.

LEE, Y. J. and FREUND, L. B.   1990b   Private communication.

MURTY, M. V. R. K.   1978   In *Optical Shop Testing* (edited by D. MALACARA), Chap. 4. J. Wiley, New York.

PRESS, W. H., FLANNERY, B. P.,   1986   *Numerical Recipes*, Chap. 14. Cambridge Uni-
    TEUKOLSKY, S. A. and   versity Press, Cambridge.
    VETTERLING, W. T.
RAVI-CHANDAR, K. and   1984   *Int. J. Fracture* **35**, 247.
    KNAUSS, W. G.
ROSAKIS, A. J. and   1986   *Int. J. Solids Struct.* **22**, 121.
    RAVI-CHANDAR, K.
ROSAKIS, A. J. and   1985   *J. Elasticity* **15**, 347.
    ZEHNDER, A. T.
THEOCARIS, P. C. and GDOUTOS, E.   1972   *J. appl. Mech.* **39**, 91.
TIPPUR, H. V., KRISHNASWAMY, S.   1989a   Caltech Report SM89-1 (to appear in *Int. J.*
    and ROSAKIS, A. J.   *Fracture*).
TIPPUR, H. V., KRISHNASWAMY, S.   1989b   Caltech Report SM89-11 (submitted to *Int. J.*
    and ROSAKIS, A. J.   *Fracture*).